


Article

Total Component Recovery of Waste Zn-Mn Batteries via Reduction Roasting Followed by Leaching Process: In Situ Preparation of Nano-ZnO Whiskers

Wei Lv ¹, Qiuyu Li ² and Zijian Su ^{2,*} 

¹ School of Metallurgy and Environment, Central South University, Changsha 410083, China; lvweicsu@163.com

² School of Minerals Processing & Bioengineering, Central South University, Changsha 410083, China; 235607004@csu.edu.cn

* Correspondence: suzijian@csu.edu.com

Abstract: Waste Zn-Mn batteries represent a significant contributor to e-waste, which is typically a hazardous material. Furthermore, Zn-Mn batteries possess more valuable metals than primary ore minerals, making them a crucial secondary resource for Zn and Mn extractive metallurgy. Current hydrometallurgy techniques primarily use acids as leaching agents, and the products are then purified by precipitating, extraction, etc. However, the Mn-Zn spinel formed in spent batteries exhibits exceptional structural stability, which can only be dissolved under strong acidic conditions. Therefore, eliminating the spinel's effects helps improve recovery efficiency. This study introduces an innovative approach for selectively recovering Zn and Mn from spent batteries by integrating reduction roasting with acid leaching, utilizing spent graphite electrodes as environmentally friendly reductants. Meanwhile, the effect of roasting and leaching on recovery efficiency is explored, as well as the phase transformation of Zn-Mn oxides during the total component recovery process. In addition, high-value-added products, nano-ZnO whiskers, are in situ synthesized via a two-stage atmosphere-controlled process. Finally, Mn and Zn recoveries of 99.8% and 99.5% are obtained under optimal conditions, and hexagonal nano-ZnO with a crystallinity of 99.9% with a grain size of 46.3 nm is synthesized successfully.

Keywords: spent Zn-Mn batteries; Mn-Zn spinel; thermomechanical analysis; reducing volatility; leaching process; valuable component recovery; nano-ZnO



Academic Editor: Ilhwan Park

Received: 25 January 2025

Revised: 13 February 2025

Accepted: 25 February 2025

Published: 27 February 2025

Citation: Lv, W.; Li, Q.; Su, Z. Total Component Recovery of Waste Zn-Mn Batteries via Reduction Roasting Followed by Leaching Process: In Situ Preparation of Nano-ZnO Whiskers. *Metals* **2025**, *15*, 256. <https://doi.org/10.3390/met15030256>

Copyright: © 2025 by the authors. Licensee MDPI, Basel, Switzerland. This article is an open access article distributed under the terms and conditions of the Creative Commons Attribution (CC BY) license (<https://creativecommons.org/licenses/by/4.0/>).

1. Introduction

Primary alkaline batteries (predominantly Zn-Mn batteries) are the most widely applied battery type, with maximum productivity due to their portability and low price [1]. It was reported that in the year 2022, about 40 billion Zn-Mn batteries were produced in China, which consumed more than 0.2 million tons of refined zinc and 0.5 million tons of manganese sulfate [2]. However, the life cycle of Zn-Mn batteries is only 0.5 to 2 years; thus, a million tons of spent batteries are generated annually. Spent batteries are typically hazardous substances due to their high contents of mercury, cadmium, lead, zinc, fluorine, etc. [3], which brings huge environmental risks. This is especially the case for zinc, which has been confirmed as having a heavy metal contamination risk [4] and extremely easily accumulates in plants and animals [5].

The industrially recoverable grade of zinc and manganese is only ~3.0 wt.% and ~20 wt.%, and Zn/Mn is extracted by physical mineral processing and metallurgical processes. Conventional zinc-manganese extraction methodologies are always long processes,

with high energy consumption and CO₂ emissions. Native zinc–manganese-bearing resources will also be exhausted over the next few years; hence, more scholars seek reusable sources and extraction methods from secondary metals [6]. Additionally, the content of valuable metals (Mn and Zn) in batteries is much higher than in primary ore. During the past few decades, scholars have paid more attention to the comprehensive utilization of Zn/Mn from waste Zn-Mn batteries [7,8].

Hydrometallurgical processes have been extensively used for the recovery of valuable metallic constituents from spent batteries [2]. It is usually necessary to utilize strong acids like nitric acid, sulfuric acid, and hydrochloric acid and then purify the product by adjusting the pH, precipitation, extraction, etc. [9,10]. However, phase transformation proceeds during the electrochemistry discharge process, and part of the MnO₂ translates into Mn-Zn spinel [11], which is difficult to dissolve under normal conditions. Hence, a high-temperature condition, pressurized oxygen leaching, organic acid medium, and electrolytic technology have also been taken into consideration [6]. However, the production of acid waste liquids and strict equipment requirements have limited the production applications of hydrometallurgy processes [12,13].

The pyrometallurgy process seems like an efficient technology to dispose of waste batteries on a large scale [14], and Zn-Mn batteries are usually used as raw materials for zinc recovery or manganese smelting. Metallic zinc is a volatile substance, which can be recovered under carbon thermal reduction in a rotary kiln or rotary hearth furnace [15,16]. In addition, the vacuum metallurgy process can decrease the melting point of metallic substances, which provides an environmentally friendly metallurgical recycling method. However, large vacuum metallurgy equipment has high requirements, which are hard to achieve [17]. The recovery of valuable metals (Sn, In, etc.) from secondary e-wastes through a chemical vapor transport process under controlled atmospheric conditions has also been reported [18]. Furthermore, the negative electrode materials of graphite in Zn-Mn batteries were found to be a high-quality reducing agent for the reduction process [19].

Therefore, an innovative process for the efficient recovery of Zn and Mn from spent Zn-Mn batteries is developed here. The phase transformation of Zn and Mn during the recycling process is systematically characterized by thermomechanical analysis, XRD, ICP, etc. In addition, nano-ZnO is synthesized in situ by a two-stage chemical vapor transport process. Generally, in this study, waste Zn-Mn batteries are resourcefully utilized and disposed of while retaining their high value.

2. Materials and Methods

2.1. Materials

The black mass derived from spent Mn-Zn alkaline batteries (AA LR6, 1.5 V) was procured from Fujian Nanping Nanfu Battery Co., Ltd., in Nanping, Fujian Province, China.

The major chemical compositions given in Table 1 were given by XRF (X-ray Fluorescence, Axios mAX) and ICP-AES (Inductively Coupled Plasma-Atomic Emission Spectrometry, IRIS Intrepid II XSP). It can be seen from Table 1 that the washed battery powders exhibited total Mn and Zn contents of 60.10 wt.% and 14.73 wt.%, respectively. Moreover, major soluble salt impurities were removed after the water-washing process, and the impurity elements (K, Ba, Mg, Fe, Cl, Al, and Fe) with low contents were found in the raw materials. The XRD analysis of the black battery powder shown in Figure 1 confirms the exclusive presence of Mn₃O₄ and ZnMn₂O₄, indicating complete conversion of MnO₂ via electrochemical reactions in the Zn-MnO₂ system. The diffraction peaks of graphite (electrode materials) are also found in Figure 1, which identified with the C content in Table 1 and can be used as a solid reductant during the roasting process. In addition,

the experimental water was deionized water, and the sulfuric acid (Sinopharm Chemical Reagent Co., Ltd., Shanghai, China) was analytically pure.

Table 1. Main chemical compositions of raw materials (wt.%).

Mn	Zn	C	K	Ba	Mg	Cl	Al	Fe
60.10	14.73	8.31	0.56	0.22	0.03	0.01	0.02	0.11

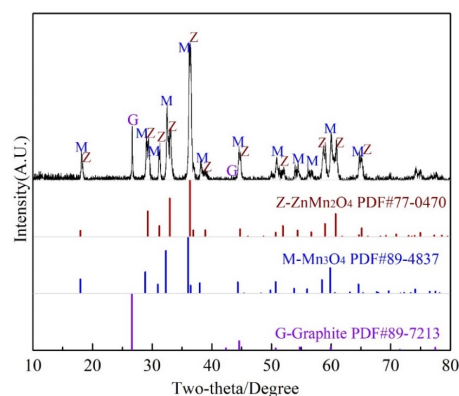


Figure 1. XRD analysis of the black powder from the cleaned Mn-Zn batteries.

2.2. Methods

Waste Zn-Mn batteries were electrically discharged and then dismantled to remove the external backing of plastic and ferrous components. After that, the black powders were washed using deionized water to remove the electrolytes, which contained ammonia chloride. Finally, the materials were ground to below 0.074 μm screen 100, and the graphite materials were ground and mixed well.

Experiments on reduction roasting were carried out in a vertical tube furnace including two temperature zones. For every test, 10.000 ± 0.002 g of the sample was placed in a corundum construction basket and then sent to the target temperature zone of the furnace for a certain time. During the roasting process, nitrogen gas was inlet into the reactor to purge residual oxygen and maintain an inert reaction environment. After roasting, the cooled sample was weighed again and then ground until all particles passed through a 0.074 mm sieve. Next, the sample was put into a 250 mL conical flask and leached with diluted sulfuric acid in a water bath, and the details of this process were reported in the previous research [20]. Finally, the solution was filtrated; then, ICP was used to assess the Mn content, and the leaching efficiency of Mn was calculated. All leaching experiments were conducted in triplicate to ensure data reliability and minimize experimental errors.

2.3. Analysis and Characterizations

Thermodynamic calculations were performed using FactSage 8.2 software (Thermfact/CRCT, Montreal, QC, Canada; GTT-Technologies, Herzogenrath, Germany). The crystalline phase compositions of samples were characterized by X-ray diffraction (XRD) using a Bruker D8 advance diffractometer (Bruker, Karlsruhe, German, using Cu K α radiation). Scans were performed in the 2θ range of 10° to 80° with a scanning step of 0.02° and a scan rate of $5^\circ/\text{min}$. Phase identification was accomplished by Jade 9.0 software. The micromorphology of samples was examined using a field-emission scanning electron microscope (SEM, Tescan MIRA3, TESCAN, Brno, Czech Republic). The sample microstructure was also examined by transmission electron microscopy (TEM, JEM-2100F, JEOL Ltd., Tokyo, Japan). X-ray photoelectron spectroscopy (XPS, ESCALAB 250Xi, ThermoFisher-VG Scientific, Waltham, MA, USA) was used to determine the sample surface chemical compo-

sition and oxidation states. Following data fitting, the spectral results underwent charge correction by referencing the C-C component in the C1s fit at 284.8 eV.

3. Results and Discussion

3.1. Thermodynamic Analysis of Zn-Mn Batteries During the Reduction Roasting and Leaching Process

In this section, the reduction of the Zn-Mn oxides during the roasting process and the E-pH analysis of the Zn-Mn oxides under the acid leaching process are analyzed, respectively. The results demonstrate that the recovery process is feasible.

3.1.1. Reduction of Zn-Mn Oxides During the Roasting Process

The principal reactions involving the Mn and Zn oxides and the corresponding ΔG_T^θ -T equations during the roasting and leaching processes are systematically summarized in Table 2. The thermodynamic calculations revealed both direct reduction and indirect reduction, as Equations (1)–(12) show. As presented in Table 2, the Zn-bearing oxides were easily reduced to metallic Zn and gasified. The reaction was then conducted under a constant pressure of 1 atm (p^θ), during which the reduction products of Zn(g) established a specific partial pressure, significantly influencing the phase transformation of ZnO. Accordingly, the predominance phase diagram of Zn(g) and MnO_x was calculated and is depicted in Figure 2, based on the thermodynamic relations ($\Delta G_T^\theta = -RT \ln K^\theta$).

Table 2. The ΔG_T^θ -T relationship of corresponding reactions.

Equations	Reaction Equations	ΔG_T^θ -T (kJ/mol)
(1)	$ZnO + C = CO_{(g)} + Zn_{(g)}$	$\Delta G_T^\theta = 362.5 - 0.296T$
(2)	$2MnO_2 + C = CO_{(g)} + Mn_2O_3$	$\Delta G_T^\theta = -27.4 - 0.193T$
(3)	$3Mn_2O_3 + C = CO_{(g)} + 2Mn_3O_4$	$\Delta G_T^\theta = -10.8 - 0.168T$
(4)	$Mn_3O_4 + C = CO_{(g)} + 3MnO$	$\Delta G_T^\theta = 115.7 - 0.207T$
(5)	$MnO + C = CO_{(g)} + Mn$	$\Delta G_T^\theta = 274.5 - 0.164T$
(6)	$C + CO_{2(g)} = 2CO_{(g)}$	$\Delta G_T^\theta = 170.9 - 0.175T$
(7)	$ZnO + CO_{(g)} = Zn_{(g)} + CO_{2(g)}$	$\Delta G_T^\theta = 191.6 - 0.121T$
(8)	$2MnO_2 + CO_{(g)} = Mn_2O_3 + CO_{2(g)}$	$\Delta G_T^\theta = -198.3 - 0.018T$
(10)	$3Mn_2O_3 + CO_{(g)} = 2Mn_3O_4 + CO_{2(g)}$	$\Delta G_T^\theta = -183.7 + 0.009T$
(11)	$Mn_3O_4 + CO_{(g)} = 3MnO + CO_{2(g)}$	$\Delta G_T^\theta = -55.2 - 0.033T$
(12)	$MnO + CO_{(g)} = Mn + CO_{2(g)}$	$\Delta G_T^\theta = 103.6 + 0.011T$
(13)	$4MnO + 8H^+ = 4Mn^{2+} + 4H_2O$	$\Delta G_T^\theta = -415.5 + 0.248T$
(14)	$2Mn_2O_3 + 8H^+ = 4Mn^{2+} + 4H_2O + O_{2(g)}$	$\Delta G_T^\theta = -99.3 + 0.026T$
(15)	$4MnO_2 + 8H^+ = 4Mn^{2+} + 4H_2O + 2O_{2(g)}$	$\Delta G_T^\theta = 4.6 - 0.190T$
(16)	$4ZnO + 8H^+ = 4Zn^{2+} + 4H_2O$	$\Delta G_T^\theta = -273.2 + 0.327T$

As presented in Figure 2, the manganese oxides were reduced stepwise in the order of $MnO_2 \rightarrow Mn_2O_3 \rightarrow Mn_3O_4 \rightarrow MnO \rightarrow Mn$. MnO_x was easily reduced to MnO in the presence of carbon thermal and CO- CO_2 reduction conditions; however, the reduction of MnO to metallic Mn was quite difficult. The reduction of MnO could proceed above 1673 K under carbothermic reduction. It can be found, as shown in Figure 2, that the reduction of ZnO to metallic Zn was relatively easy in the range of 600–1600 K. Nonetheless, the decrease in Zn(g) partial pressure led to a significant expansion of the phase coexistence region. Hence, during the roasting process, as shown in Figure 2, the newly generated Zn(g) might be removed by the gas flow of the reduction gases, lowering the reaction temperature and facilitating the reduction of Equations (1) and (7). As shown in Figure 1, the crushed

graphite electrode was a superior reducing agent; hence, an autocatalytic reduction roasting was proposed.

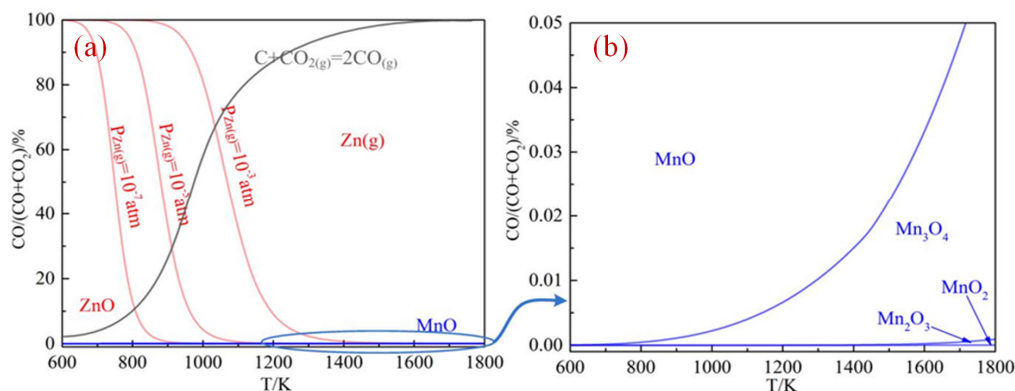


Figure 2. Gas-phase equilibrium diagram of reduction of (a) Zn and Mn oxides and (b) Mn oxides.

3.1.2. E-pH Analysis of Zn-Mn Oxides Under Acid Leaching Process

The thermodynamic equilibrium E-pH diagram for the Zn-Mn-H₂O system was computationally generated using FactSage 8.2 software, with the resultant phase stability domains presented in Figure 3. Only Mn²⁺ and Zn²⁺ can be soluble under an acid environment. The stable coexistence region of Mn²⁺/Zn²⁺ (shadow area in Figure 3) was wide, indicating the separation was difficult during the leaching process. The dissolved pH was greatly affected by temperature, while the value was 5.8 at a room temperature of 25 °C (Figure 4a) and 4.1 at 100 °C (Figure 4b). Previous studies have proved that solubility under an acidic medium can be expressed as Mn₂O₃ < ZnMn₂O₄ < Mn₃O₄ < ZnO < MnO [20,21]. As shown in Figure 1, the primary phase composition was ZnMn₂O₄, which proved challenging to recover using a sulfuric acid leaching process. The reduction of the Mn-Zn spinel to MnO and Zn(g) under suitable conditions was the crucial element for the flexible use of the Zn-Mn batteries, according to the thermodynamics analysis. After that, MnO can be leached in acidic solutions and Zn can be extracted from the volatile products.

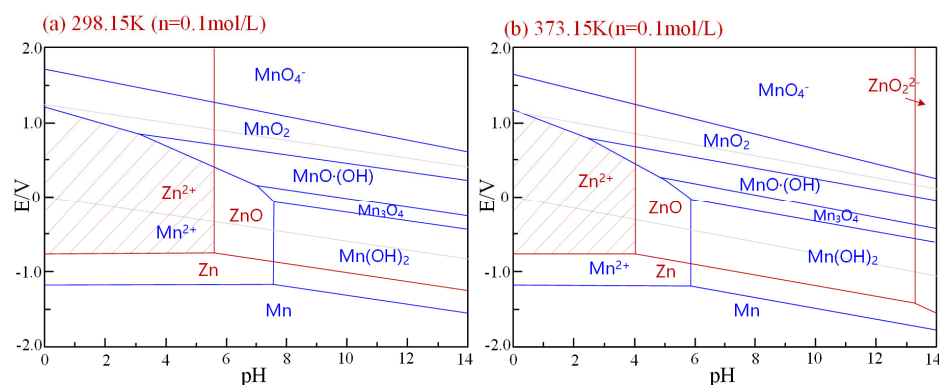


Figure 3. E-pH diagrams of the Zn-Mn-H₂O system (a) at 298.15 K and (b) at 373.15 K.

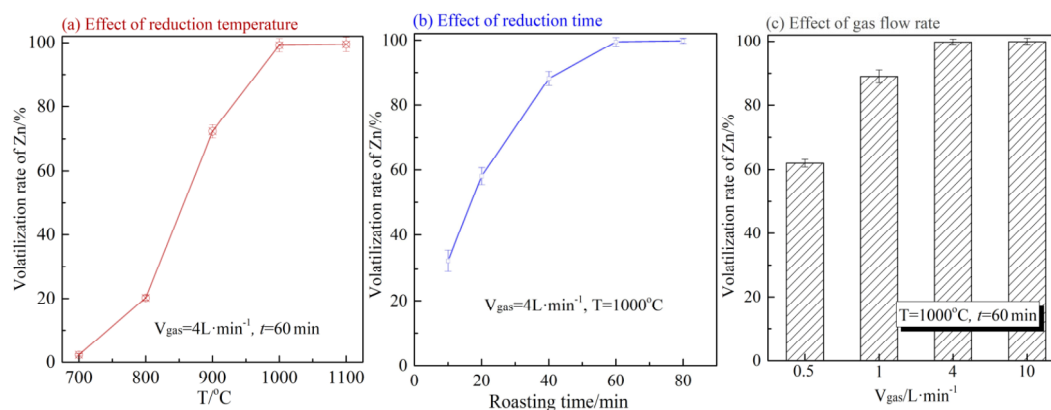


Figure 4. Effect of reduction condition on the volatilization of Zn: (a) effect of reduction temperature, (b) effect of reduction time, (c) effect of gas flow rate.

3.2. Recovery of Zn During the Autocatalytic Reduction Roasting Process

By controlling the temperature and atmosphere, zinc was first reduced and volatilized to metallic zinc and then oxidized to ZnO. The effect of roasting conditions on the Zn volatilization and the preparation of nano-ZnO whiskers were analyzed.

3.2.1. Effect of Roasting Condition on the Zn Volatilization

As illustrated in Figure 3, the reduction of Zn-Mn oxides was controlled by the reduction temperature and partial pressure of Zn(g). The effects of roasting parameters including the reduction temperature, roasting time, and gas flow rate of nitrogen on the volatilization of Zn were examined, and the results are presented in Figure 4. As shown in Figure 4a, the Zn volatilization exhibited a pronounced temperature dependence. The Zn volatilization rate increased exponentially from 2.3 wt.% to 99.2 wt.% as the temperature rose from 700 °C up to 1000 °C and then was almost unchanged as the temperature further increased to 1100 °C. Figure 4b illustrates the effect of reduction time on the Zn volatilization ratio, and the sample was roasted at 1000 °C in the range of 10–80 min. The Zn volatilization ratio increased sharply by prolonging the reduction time from 10 min to 60 min and then varied slightly. Hence, the optimal roasting time was fixed at 60 min. It was noteworthy that the Zn volatilization was also promoted by a higher gas flow rate (Figure 4c). The results indicated that a higher nitrogen flow rate could decrease the partial pressure of Zn(g), which promoted the reduction of Zn-bearing oxides (as shown in Figure 2).

3.2.2. Phase Transformations of Mn-Zn Oxides During the Roasting Process

To further investigate the phase transformation of Mn-Zn oxides during the reduction roasting process, an XRD analysis of the roasted products was conducted, and the results are shown in Figure 5.

As presented in Figure 6, the major mineral constituents in the roasted products were MnO, which indicated the superior reducibility of graphite in the batteries. Virtually all of the Zn-Mn spinels were reduced to MnO and Zn above 700 °C, as found using Equations (1)–(4). However, the reduction of MnO to metallic Mn was difficult under normal conditions (Equations (5) and (12)), and MnO was the final reduction phase in the reduction products. The results further verified the results in Figure 5, that a higher reduction temperature promoted the reduction of the Zn-bearing spinel and the gasification of zinc. In addition, the diffraction peaks of Mn₇C₃ were found at 1000–1100 °C, which was in line with our previous studies [22]. The reaction of MnO + C → Mn₇C₃ + CO can proceed beyond 1065 °C under strong reduction conditions. Nevertheless, the Mn₇C₃'s leachability

was significantly worse than the MnO's, which could hinder Mn recovery throughout the leaching process.

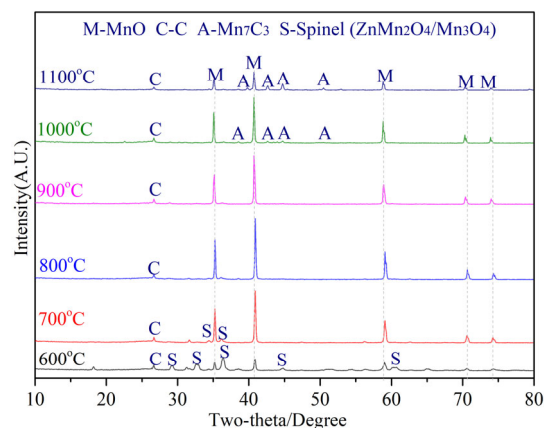


Figure 5. XRD analysis of the roasted products under different temperatures.

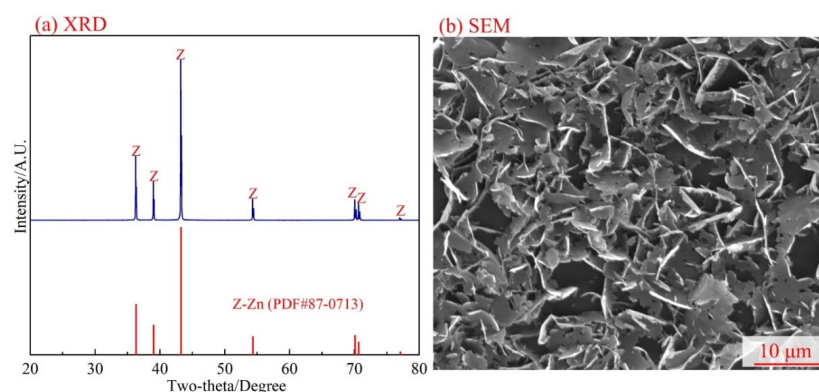


Figure 6. Phase analysis of volatile products: (a) XRD analysis, (b) SEM analysis.

The volatile products' XRD patterns (shown in Figure 6a) showed the exclusive formation of high-purity metallic zinc at 1000 °C with no discernible impurity phases. Further chemical analysis indicated that the Zn content of the volatile products was 96.1 wt.%, and trace amounts of impurities were oxygen and carbon. The SEM results shown in Figure 6b demonstrate that the zinc was easy to condense, crystallize, and agglomerate. Then, the crystal growth was disordered, and plates in the size range of 5–50 μm were obtained. However, the physical and chemical indicators are less than the first-grade products for the national standard of zinc powder (GB/T 6890-2012) [23].

3.2.3. In Situ Preparation of Nano-ZnO Whiskers

According to earlier research, nano-ZnO is a high-value product that can be synthesized by the CVT process [24]. The gaseous-phase Zn generated by the reduction roasting process (in Section 3.1.1) was found to be appropriate for making ZnO due to its high purity and activity. A two-stage oxidation process is proposed to prepare ZnO in this section. First, the oxidation thermodynamics of zinc to ZnO ($\text{Zn}_{(g)} + \text{O}_{2(g)} = \text{ZnO}$, Equation (13)) was analyzed and is presented in Figure 7.

The results in Figure 7 illustrate that the Gibbs's free energy of Equation (13) was negative under various $\text{Zn}_{(g)}$ partial pressures. Hence, the experimental facility of a double temperature zone tube furnace with different atmospheres was designed, as shown in Figure 8, and the gas flow of the O_2/N_2 mixture was introduced to oxidize the newly formed $\text{Zn}_{(g)}$.

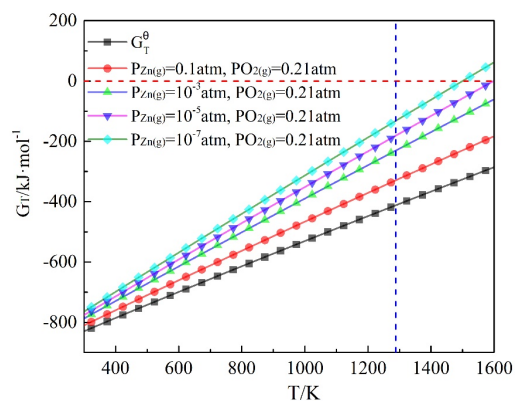


Figure 7. The ΔG_T^0 -T relationship of $\text{Zn(g)} + \text{O}_2(\text{g}) = \text{ZnO}$ under various Zn(g) partial pressures.

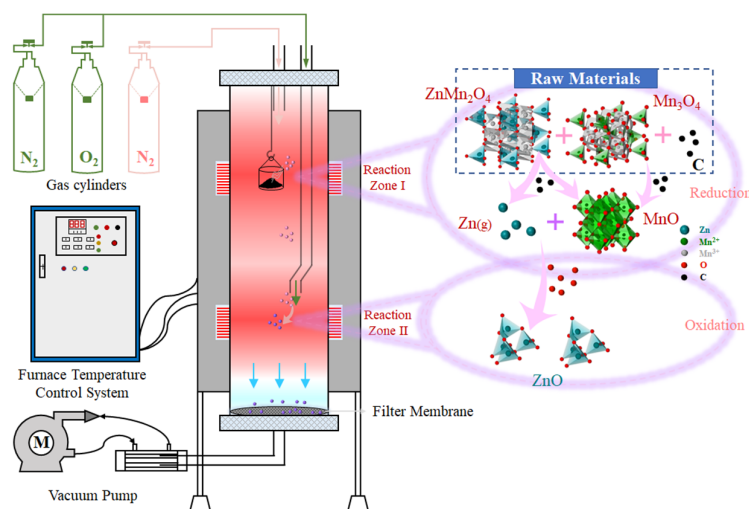


Figure 8. Double temperature zone tube furnace with different designed atmosphere.

The following experimental parameters were established based on the thermodynamic study mentioned above: the first stage was roasting at 1000 °C under a high-purity nitrogen atmosphere with a gas flow rate of 4 L/min, and the second stage was the addition of inlet mixed gas of $\text{O}_2 + \text{N}_2$. The total O_2 content in the second stage was fixed at 0.1–10 vol.% with a gas flow rate of 5 L/min. Then, the final products were collected and are analyzed in Figures 9 and 10.

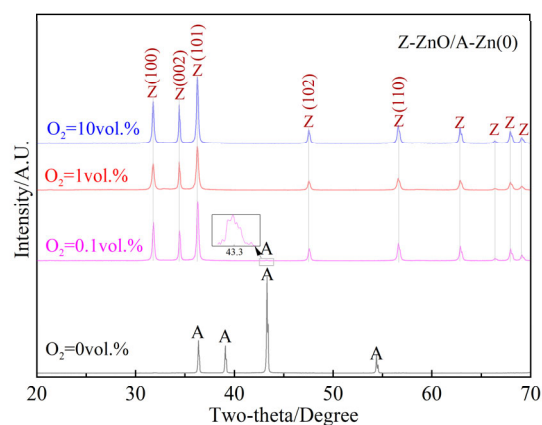


Figure 9. Effect of O_2 content on the formation of nano-ZnO products.

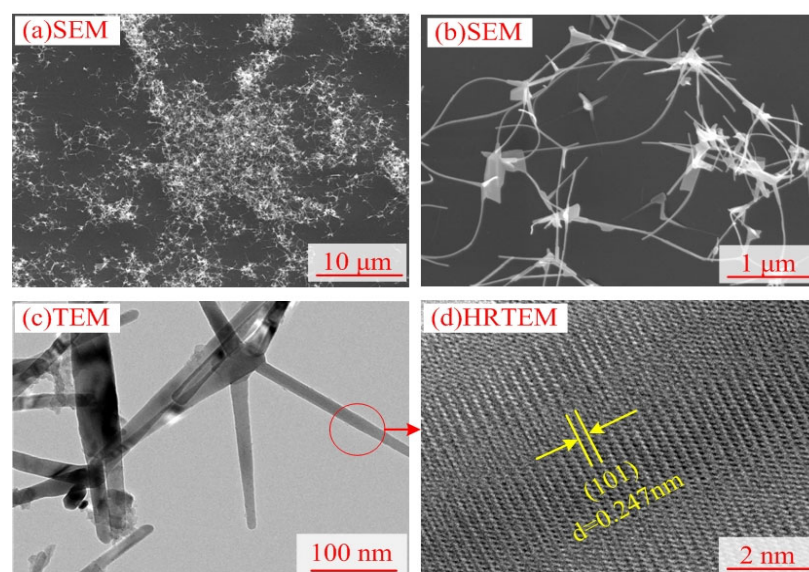


Figure 10. Microstructure of synthetic nano-ZnO whiskers (second stage of 1000 °C under 10% O₂ atmosphere): (a) SEM analysis (10 μm), (b) SEM analysis (1 μm), (c) TEM (100 nm), (d) HRTEM (2 nm).

The results in Figure 10 confirm that the gaseous Zn was easily oxidized to ZnO under a comparatively low O₂ atmosphere. The main phase compositions were only ZnO under a 0.1–10 vol.% O₂ content. It can be found by careful observation that weak diffraction peaks of metallic Zn existed under 0.1 vol.%, while the peaks were completely obliterated under the 1–10 vol.% O₂ atmosphere. The diffraction peaks in Figure 9 are well matched with the standard card (ZnO PDF# 89-1397), with the hexagonal crystal structure and the space groups of P6₃mc (186) (90° × 90° × 90°). The grain size of the ZnO was fine-grained at 55.2 nm (1% O₂) and 46.3 nm (10% O₂) calculated based on the *Scherrer* formula. In addition, the crystallinity of the ZnO was with a theoretical purity of more than 99.9%, analyzed using Jade 9.0. The specific surface area of the products was measured as 82.5 m²/g, which further illustrated that the nano-ZnO exhibited fine granularity. The quality of the products meets the requirements of first-grade products (GB/T 19589-2004) [25].

The morphology of the CVT nano-ZnO was characterized by SEM and TEM analysis, and the results are shown in Figure 10. The particle size of ZnO in Figure 10a was relatively small and uniform, and the tetrapod nano-ZnO with a length of 1–5 μm (Figure 10b) was with excellent dispersity. The TEM results in Figure 10c illustrate that the whisker width of the ZnO was 10–30 nm, and the length–width ratio was in the range of 50–200. Furthermore, the HRTEM image (Figure 10d) of the nano-ZnO displays obvious lattice fringes. The results demonstrated that the synthetic nano-ZnO was in good crystal condition, with the dominant (101) crystallographic plane observed at $2\theta = 36.26^\circ$ and a corresponding interlayer spacing of 0.247 nm.

XPS was employed to investigate the chemical state of Zn and O in the nano-ZnO, and the results are demonstrated in Figure 11. As shown in Figure 11b, the Zn 2p photoelectron peak was well matched with the peaks of Zn²⁺ reported in previous literature, and the chemical bonding energies of Zn 2p 1/2 and Zn 2p 3/2 were 1044.5 eV and 1021.4 eV, respectively [26,27]. On the other hand, Figure 11c shows the peaks of the O 1s high-resolution spectra, of which the binding energy shifted obviously from 531.9 eV of adsorbed oxygen (O_α) to 531.0 eV of defective oxygen (O_D) and 530.1 eV of lattice oxygen (O_L). Furthermore, the oxygen vacancy in the nano-ZnO was in favor of the photoelectric properties [28,29]. The energy gap of the nano-ZnO was 3.22 eV by ultraviolet analysis, which can be used for photocatalysis.

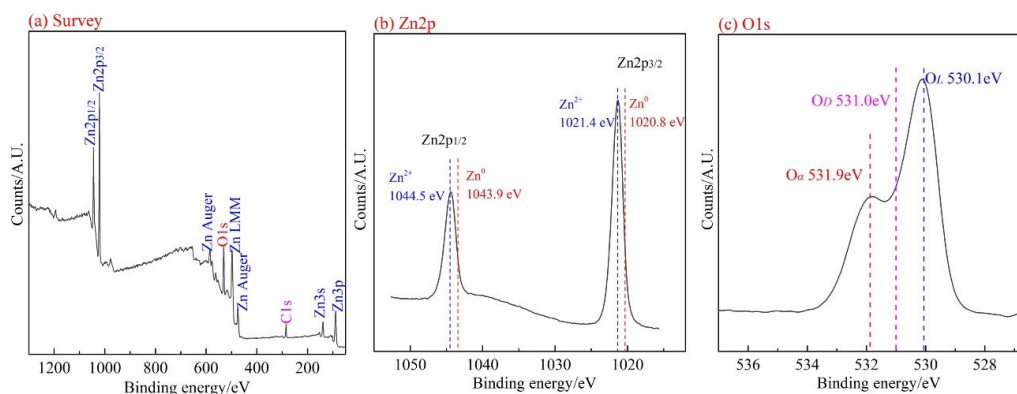


Figure 11. XPS analysis of nano-ZnO whiskers (second stage of 1000 °C under 10% O₂ atmosphere): (a) survey, (b) Zn2p, (c) O1s.

3.3. Leaching Behavior of Mn from the Reduction-Roasted Residues

Based on the above investigation, the primary phase of the roasted residues was MnO, which can be recovered by an acid-leaching procedure [20]. Additionally, the leaching process of MnO has been thoroughly investigated. In this section, the primary evaluation metric is the leaching efficiency of Mn, and the Mn-rich solutions can also undergo additional processing to yield compounds like MnSO₄. The ideal Zn volatilization rate during the reduction roasting process was attained with a roasting time of 60 min and a gas flow rate of 4 L/min. As a result, throughout the leaching process, all roasting parameters except temperature were set. Additionally, the liquid–solid ratio of 5:1, stirring rate of 300 rpm, and leaching time of 60 min were selected during the leaching process, referring to a previous group's research [30].

According to the results shown in Figure 12a, the leaching of Mn from the roasted residues was significantly impacted by the roasting temperature. The Mn leaching efficiency of the unroasted raw material was only 21.3 wt.%, which was on account of the poor solubility of the Zn-Mn spinels. As the roasting temperature rose from 700 °C to 1000 °C, the Mn leaching ratio rose dramatically from 68.3% to 99.8%. Unexpectedly, the Mn leaching efficiency dropped to 88.2% when the roasting temperature was raised to 1100 °C. The conversion of manganese oxides to MnO was promoted by increasing the roasting temperature. However, the decrease in Mn leaching efficiency at 1100 °C was caused by the generation of Mn₇C₃, which has lower leaching properties than any other manganese oxides [31].

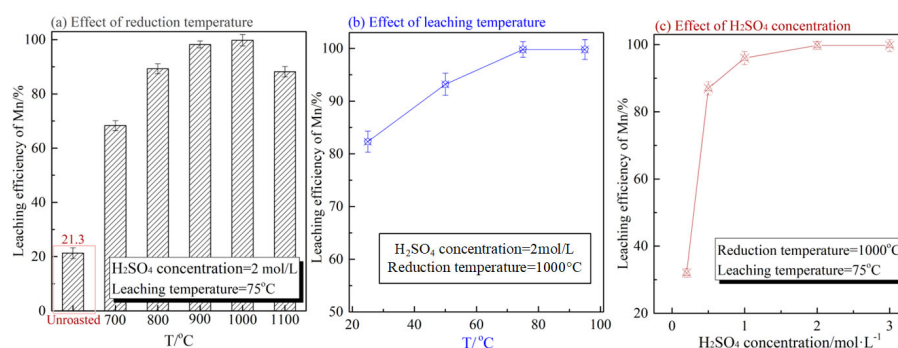


Figure 12. Leaching behavior of Mn from the roasted residues: (a) effect of reduction temperature, (b) effect of leaching temperature, (c) effect of H₂SO₄ concentration.

Based on the above results, the Zn-Mn oxides were reduced at higher than 700 °C, and MnO was leached at a pH value lower than 4. The single-variable experiments were conducted in Section 3.2.1. Single-variable experiments are commonly used experimental

methods in the field of metallurgy, and temperature is the most important condition during the reaction. The optimized parameters were determined through a systematic investigation as follows: roasting at 1000 °C for 60 min, followed by leaching with 2 mol/L H₂SO₄ at 75 °C for 60 min under a liquid–solid ratio of 5:1 and an agitation speed of 300 rpm. As shown in Table 3, nano-ZnO with a purity of 99.9 wt.% was obtained, and the leaching recovery of Mn was as high as 99.8%. The Mn-bearing leaching solutions can be used in the production of electrolytic manganese and the preparation of battery-grade manganese sulfate [32].

Table 3. The results obtained under optimal conditions.

	Grade/wt.%		Recovery/wt.%	
	Mn	Zn	Mn	Zn
Raw materials	60.10	14.73	-	-
Volatile products	-	99.9	-	99.5
Leaching solution	0.12 g/mL	-	99.8	-

4. Conclusions

This study proposed a novel two-stage process involving autocatalytic reduction roasting coupled with hydrometallurgical leaching for the selective separation and recovery of Zn and Mn from spent battery materials. The following conclusions were drawn:

(1) Mn–Zn oxides of 60.10 wt.% Mn and 14.73 wt.% Zn were obtained from the waste batteries after the discharge and washing process. The main phases of the spinels (Mn₃O₄ and ZnMn₂O₄) were difficult to recover by the direct acid leaching process. In addition, graphite electrodes also remained in the black powder and can be used as a solid reducing agent.

(2) The thermodynamic analysis indicated that manganese oxides were reduced stepwise in the order of MnO₂ → Mn₂O₃ → Mn₃O₄ → MnO → Mn. The reduction of MnO_x to MnO was easy at relatively low temperatures and had reduction potential. The solubility under an acidic medium can be expressed as Mn₂O₃ < ZnMn₂O₄ < Mn₃O₄ < ZnO < MnO. The crucial process for the separation of Zn and Mn was the selective reduction of the Zn–Mn spinel to MnO and gaseous Zn; then, Zn could be recovered from the outlet gas and MnO was easily leached in a weak acid solution.

(3) A two-stage roasting process was used to investigate the CVT method: first-stage roasting at 1000 °C with nitrogen at a gas flow rate of 4 L/min followed by a second-stage roasting at 1000 °C with a gas flow rate of 5 L/min in an environment containing 10% O₂. Ultimately, hexagonal ZnO with a crystallinity of 99.9% and a grain size of 46.3 nm was produced, along with high-value nano-ZnO whiskers.

(4) Under the optimal process parameters of the roasting temperature of 1000 °C for 60 min, the Zn was recovered at 99.5 wt.%, and through subsequent leaching at 75 °C with a liquid–solid ratio of 5:1, 2 mol/L H₂SO₄, a 300 rpm stirring rate, and a 60 min duration. Under these parameters, the manganese leaching efficiency achieved 99.8%. Notably, roasting temperatures above 1000 °C promoted the formation of Mn₇C₃, which reduced the leaching efficiency of Mn.

Author Contributions: Conceptualization: W.L.; methodology: W.L. and Q.L.; investigation: W.L., Z.S. and Q.L.; data curation: Q.L.; writing—original draft preparation: W.L.; writing—review and editing: Z.S.; supervision: W.L.; funding acquisition: Z.S. All authors have read and agreed to the published version of the manuscript.

Funding: This study received funding by the National Key R&D Program of China (NO. 2024YFC2910800) and the Science and Technology Innovation Program of Hunan Province (No. 2024RC3022).

Data Availability Statement: The original contributions presented in this study are included in the article. Further inquiries can be directed to the corresponding author.

Conflicts of Interest: All authors declare that the research was conducted in the absence of any commercial or financial relationships that could be construed as potential conflicts of interest.

References

1. Luo, H.; Liu, B.; Yang, Z.; Wan, Y.; Zhong, C. The Trade-Offs in the Design of Reversible Zinc Anodes for Secondary Alkaline Batteries. *Electrochem. Energy Rev.* **2022**, *5*, 187–210. [\[CrossRef\]](#)
2. Tran, L.-H.; Tanong, K.; Jabir, A.D.; Mercier, G.; Blais, J.-F. Hydrometallurgical Process and Economic Evaluation for Recovery of Zinc and Manganese from Spent Alkaline Batteries. *Metals* **2020**, *10*, 1175. [\[CrossRef\]](#)
3. Ma, S.; Liao, C.-Z.; Leung, K.-M.; Zhou, Y.; Shih, K. Self-Consumed Strategy to Reuse Cathode Residue for Zn Stabilization in Spent Batteries: Structural Properties and Metal Stabilization Effect. *Waste Manag.* **2023**, *168*, 272–280. [\[CrossRef\]](#) [\[PubMed\]](#)
4. Luo, X.; Wu, C.; Lin, Y.; Li, W.; Deng, M.; Tan, J.; Xue, S. Soil Heavy Metal Pollution from Pb/Zn Smelting Regions in China and the Remediation Potential of Biomineralization. *J. Environ. Sci.* **2023**, *125*, 662–677. [\[CrossRef\]](#)
5. Jiang, Y.; Wei, C.; Jiao, Q.; Li, G.; Alyemeni, M.N.; Ahmad, P.; Shah, T.; Fahad, S.; Zhang, J.; Zhao, Y.; et al. Interactive Effect of Silicon and Zinc on Cadmium Toxicity Alleviation in Wheat Plants. *J. Hazard. Mater.* **2023**, *458*, 131933. [\[CrossRef\]](#)
6. Gao, P.; Yuan, P.; Yue, T.; Zhao, X.; Shen, B. Recycling Metal Resources from Various Spent Batteries to Prepare Electrode Materials for Energy Storage: A Critical Review. *J. Energy Storage* **2023**, *68*, 107652. [\[CrossRef\]](#)
7. Liu, M.; Zhang, K.; Liang, Y.; Yang, Y.; Chen, Z.; Liu, W. Life Cycle Environmental and Economic Assessment of Electric Bicycles with Different Batteries in China. *J. Clean. Prod.* **2023**, *385*, 135715. [\[CrossRef\]](#)
8. Rinne, T.; Klemettinen, A.; Klemettinen, L.; Ruismäki, R.; O'Brien, H.; Jokilaakso, A.; Serna-Guerrero, R. Recovering Value from End-of-Life Batteries by Integrating Froth Flotation and Pyrometallurgical Copper-Slag Cleaning. *Metals* **2021**, *12*, 15. [\[CrossRef\]](#)
9. Łukomska, A.; Wiśniewska, A.; Dąbrowski, Z.; Kolasa, D.; Luchcińska, S.; Lach, J.; Wróbel, K.; Domańska, U. Recovery of Zinc and Manganese from “Black Mass” of Waste Zn-MnO₂ Alkaline Batteries by Solvent Extraction Technique with Ionic Liquids, DESs and Organophosphorous-Based Acids. *J. Mol. Liq.* **2021**, *338*, 116590. [\[CrossRef\]](#)
10. Sobianowska-Turek, A.; Szczepaniak, W.; Maciejewski, P.; Gawlik-Kobylińska, M. Recovery of Zinc and Manganese, and Other Metals (Fe, Cu, Ni, Co, Cd, Cr, Na, K) from Zn-MnO₂ and Zn-C Waste Batteries: Hydroxyl and Carbonate Co-Precipitation from Solution after Reducing Acidic Leaching with Use of Oxalic Acid. *J. Power Sources* **2016**, *325*, 220–228. [\[CrossRef\]](#)
11. Chen, B.; Miao, H.; Yin, M.; Hu, R.; Xia, L.; Zhang, C.; Yuan, J. Mn-Based Spinel Evolved from Layered Manganese Dioxides at Mild Temperature for the Robust Flexible Quasi-Solid-State Zinc-Air Batteries. *Chem. Eng. J.* **2021**, *417*, 129179. [\[CrossRef\]](#)
12. Hu, X.; Robles, A.; Vikström, T.; Väänänen, P.; Zackrisson, M.; Ye, G. A Novel Process on the Recovery of Zinc and Manganese from Spent Alkaline and Zinc-Carbon Batteries. *J. Hazard. Mater.* **2021**, *411*, 124928. [\[CrossRef\]](#) [\[PubMed\]](#)
13. Işıldar, A.; Rene, E.R.; Van Hullebusch, E.D.; Lens, P.N.L. Electronic Waste as a Secondary Source of Critical Metals: Management and Recovery Technologies. *Resour. Conserv. Recycl.* **2018**, *135*, 296–312. [\[CrossRef\]](#)
14. Wang, F.; Long, G.; Ma, K.; Zeng, X.; Tang, Z.; Dong, R.; He, J.; Shanguan, M.; Hu, Q.; Liew, R.K.; et al. Recycling Manganese-Rich Electrolytic Residues: A Review. *Environ. Chem. Lett.* **2023**, *21*, 2251–2284. [\[CrossRef\]](#)
15. Belardi, G.; Lavecchia, R.; Medici, F.; Piga, L. Thermal Treatment for Recovery of Manganese and Zinc from Zinc–Carbon and Alkaline Spent Batteries. *Waste Manag.* **2012**, *32*, 1945–1951. [\[CrossRef\]](#)
16. Buzatu, M.; Săceanu, S.; Petrescu, M.I.; Ghica, G.V.; Buzatu, T. Recovery of Zinc and Manganese from Spent Batteries by Reductive Leaching in Acidic Media. *J. Power Sources* **2014**, *247*, 612–617. [\[CrossRef\]](#)
17. Zhan, L.; Li, O.; Xu, Z. Preparing Nano-Zinc Oxide with High-Added-Value from Waste Zinc Manganese Battery by Vacuum Evaporation and Oxygen-Control Oxidation. *J. Clean. Prod.* **2020**, *251*, 119691. [\[CrossRef\]](#)
18. Su, Z.; Zhang, Y.; Han, B.; Liu, B.; Lu, M.; Peng, Z.; Li, G.; Jiang, T. Synthesis, Characterization, and Catalytic Properties of Nano-SnO by Chemical Vapor Transport (CVT) Process under CO-CO₂ Atmosphere. *Mater. Des.* **2017**, *121*, 280–287. [\[CrossRef\]](#)
19. Farzana, R.; Rajarao, R.; Hassan, K.; Behera, P.R.; Sahajwalla, V. Thermal Nanosizing: Novel Route to Synthesize Manganese Oxide and Zinc Oxide Nanoparticles Simultaneously from Spent Zn–C Battery. *J. Clean. Prod.* **2018**, *196*, 478–488. [\[CrossRef\]](#)
20. You, Z.; Li, G.; Zhang, Y.; Peng, Z.; Jiang, T. Extraction of Manganese from Iron Rich MnO₂ Ores via Selective Sulfation Roasting with SO₂ Followed by Water Leaching. *Hydrometallurgy* **2015**, *156*, 225–231. [\[CrossRef\]](#)
21. Petranikova, M.; Ebin, B.; Mikhailova, S.; Steenari, B.-M.; Ekberg, C. Investigation of the Effects of Thermal Treatment on the Leachability of Zn and Mn from Discarded Alkaline and ZnC Batteries. *J. Clean. Prod.* **2018**, *170*, 1195–1205. [\[CrossRef\]](#)
22. Liu, B.; Zhang, Y.; Su, Z.; Peng, Z.; Li, G.; Jiang, T. Thermodynamic Analysis and Reduction of MnO₂ by Methane–Hydrogen Gas Mixture. *JOM* **2017**, *69*, 1669–1675. [\[CrossRef\]](#)
23. GB/T 6890-2012; Zinc Powder. China Nonferrous Metals Industry Association: Beijing, China, 2012.

24. Colibaba, G.V. ZnO Doping Efficiency by Multivalent Metals in Complex CVT Reactions. *Solid State Sci.* **2019**, *97*, 105944. [[CrossRef](#)]
25. GB/T 19589-2004; Nano-Zinc Oxide. China Nonferrous Metals Industry Association: Beijing, China, 2004.
26. Gancheva, M.; Markova-Velichkova, M.; Atanasova, G.; Kovacheva, D.; Uzunov, I.; Cukeva, R. Design and Photocatalytic Activity of Nanosized Zinc Oxides. *Appl. Surf. Sci.* **2016**, *368*, 258–266. [[CrossRef](#)]
27. Hu, C.; Hu, X.; Li, R.; Xing, Y. MOF Derived ZnO/C Nanocomposite with Enhanced Adsorption Capacity and Photocatalytic Performance under Sunlight. *J. Hazard. Mater.* **2020**, *385*, 121599. [[CrossRef](#)]
28. Noman, M.T.; Amor, N.; Petru, M. Synthesis and Applications of ZnO Nanostructures (ZONSs): A Review. *Crit. Rev. Solid State Mater. Sci.* **2022**, *47*, 99–141. [[CrossRef](#)]
29. Yu, S.; Zhou, J.; Ren, Y.; Yang, Z.; Zhong, M.; Feng, X.; Su, B.; Lei, Z. Excellent Adsorptive-Photocatalytic Performance of Zinc Oxide and Biomass Derived N, O-Contained Biochar Nanocomposites for Dyes and Antibiotic Removal. *Chem. Eng. J.* **2023**, *451*, 138959. [[CrossRef](#)]
30. Zhang, Y.; You, Z.; Li, G.; Jiang, T. Manganese Extraction by Sulfur-Based Reduction Roasting–Acid Leaching from Low-Grade Manganese Oxide Ores. *Hydrometallurgy* **2013**, *133*, 126–132. [[CrossRef](#)]
31. Paek, M.-K.; Pak, J.-J.; Kang, Y.-B. Phase Equilibria and Thermodynamics of Mn–C, Mn–Si, Si–C Binary Systems and Mn–Si–C Ternary System by Critical Evaluation, Combined with Experiment and Thermodynamic Modeling. *Calphad* **2014**, *46*, 92–102. [[CrossRef](#)]
32. Shi, P.; Yang, S.; Wu, G.; Chen, H.; Chang, D.; Jie, Y.; Fang, G.; Mo, C.; Chen, Y. Efficient Separation and Recovery of Lithium and Manganese from Spent Lithium-Ion Batteries Powder Leaching Solution. *Sep. Purif. Technol.* **2023**, *309*, 123063. [[CrossRef](#)]

Disclaimer/Publisher’s Note: The statements, opinions and data contained in all publications are solely those of the individual author(s) and contributor(s) and not of MDPI and/or the editor(s). MDPI and/or the editor(s) disclaim responsibility for any injury to people or property resulting from any ideas, methods, instructions or products referred to in the content.